

Theoretical Model Construction of Deformation-Force for Soft Grippers Part I: Co-rotational Modeling and Force Control for Design Optimization

Huixu Dong, Haotian Guo, Sihao Yang, Chen Qiu, Jiansheng Dai, *Fellow, IEEE*, I-Ming Chen, *Fellow, IEEE*

Abstract—Compliant grippers, owing to adaptivity and safety, have attracted considerable attention for unstructured grasping in real applications, such as industrial or logistic scenarios. However, accurate construction of the mathematical model depicting the bidirectional relationship between shape deformation and contact force for such grippers, such as the Fin-Ray grippers, remains stagnant to date. To address this research gap, this article devises, presents, and experimentally validates a universal bidirectional force-displacement mathematical model for compliant grippers based on the co-rotational concept, which endows such grippers with an intrinsic force sensing capability and offers a better insight into the design optimization. In Part I of the article, we introduce the fundamental theory of the co-rotational approach, where arbitrary large deformation of beam elements can be modeled. Its intrinsic principle enables the theoretical modeling to consider various types of configurations and key design parameters with very few assumptions made. Further, a force control algorithm is proposed, providing accurate displacement estimations of the gripper under external forces with minor computational loads. The performance of the proposed method is experimentally verified through comparison with Finite Element Analysis (FEA), where the influence of four key design parameters on the gripper’s performance is investigated, facilitating systematical design optimization. Part II of this article demonstrating the force sensing capabilities and the effects of representative co-rotational modeling parameters on model accuracy is released in Google Drive¹.

Index Terms—Compliant gripper, Optimal design, Bidirectional modeling, Grasp performance

I. INTRODUCTION

GRASP is an essential capability for most robots in practical applications [1], [2]. As grasping executors, compliant grippers have an obvious advantage in grasping unstructured objects, such as soft, fragile, deformable, time-varying ones [3]–[5]. Generally, current compliant grippers can be categorized as either traditional multiple-rigid-link

Huixu Dong, Haotian Guo, Sihao Yang are with Robot Perception and Grasp Laboratory(Grasp Lab), Zhejiang University, Hangzhou 310058, China (e-mail: huixudong@zju.edu.cn). I-Ming Chen is with Robotics Research Center, Nanyang Technological University, Singapore 639798. Chen Qiu is with Maider Medical Industry Equipment Co., Ltd, China 317607. Jiansheng Dai is with Shenzhen Key Laboratory of Biomimetic Robotics and Intelligent Systems, SUSTech Institute of Robotics, Southern University of Science and Technology, Shenzhen, 518055, China, and Centre for Robotics Research, Department of Engineering, King’s College London Strand, London WC2R 2LS, UK.

¹Part II: <https://drive.google.com/file/d/12Ry3GrMrbdvVuxcGEyUSgnTnyCJRw3n/view>

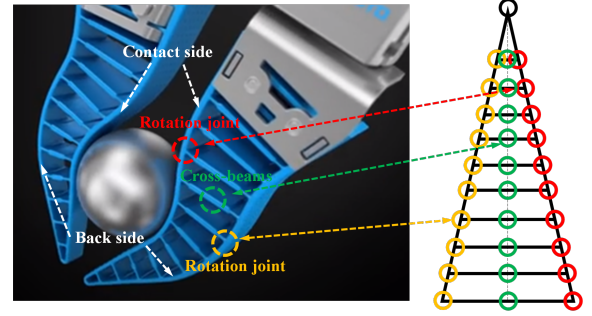


Figure 1: Festo’s soft gripper based on Fin-Ray® effect and its equivalent fin-ray structure. The green circles represent the cross-beams; the yellow circles indicate the joints of the back side and the red circles are the joints of the contact side.

grippers that perform compliant grasps or most soft grippers. To achieve compliance, rigid grippers are usually designed as under-actuated ones by combining multiple rigid links and joints with only fewer actuators [6]–[8]. Soft grippers possess superior compliant performance in grasping objects with arbitrary shapes owing to the infinite amount of Degree of Freedom (DOF). Their deformations are usually based on soft materials’ intrinsic mechanical properties and investigations mainly emphasize the gripper design [9]–[11] and actuation strategies [12]. By contrast, a Fin-Ray gripper, which is a migration from the rigid gripper to a soft one, achieved a good balance of compliance and payload and has attracted researchers’ attention[4], [13]. Figure 1 reveals a commercialized product, Festo DAHS.

Despite the abundant achievements in compliant grippers design, rare literature mentions the theoretical models for them due to either the complex parameters involved in such non-linear models or the substantial amount of assumptions and constraints. Combining kinematic and static analyses of the under-actuated four-bar driven slider-crank, Yoon et.al designs a compliant rigid gripper with optimized parameters[14]. Till’s work benefits from the modeling of the deformation of the slender legs composing the robot with continuous Cosserat rod theory. They successfully predict the unstable solutions and prevent the leg’s buckling [15]. Similarly, with the discrete-Cosserat-approach-based force-deformation modeling, Armanini et.al improves the Fin-Ray gripper design, which is able to conform to contacting surfaces, while maintaining stiffness out of its grasping plane [16]. However,

existing research tends to target a specific type of compliant grippers, and a universal mathematical model depicting the force-displacement behaviors of more grippers is still a need [3], [13], [17].

Inspired by the co-rotational concept [18], which offers an accurate compliance modeling of arbitrary large deformation of beam elements under external loads with fewer assumptions, this article first explores, presents, and experimentally verifies the construction of a universal bidirectional force-deformation mathematical model, providing insights into design optimization of compliant grippers and force sensing capability sensor-free. The Fin-Ray gripper is chosen for its generalization ability to other compliant grippers. Especially, a soft/continuum gripper can be commonly considered a Fin-Ray gripper with numerous crossbeams with low stiffness material for readily deforming. While a compliant rigid gripper with multiple joints may be regarded as a Fin-Ray gripper with several crossbeams constructed by high-stiff material.

The foremost contribution of this article is that we uniquely model and analyze the mathematical relationships between the finger deformation and contact forces through the co-rotational theory, which can be easily generalized to other compliant grippers. We highlight the novelties in Part I. **First**, we devise a computational-efficient force-deformation model for the Fin-Ray grippers based on the co-rotational concept and experimentally verify its effectiveness through comparisons with FEA. **Second**, the influence of four key design parameters for a Fin-Ray gripper on its performance is systematically investigated for design optimization. A critical insight into the optimized trade-off of performance in specified applications has been provided. In Part II, the intrinsic force sensing capability based on the deformation-force model is explored.

II. MODELING AND ANALYSIS

A. Co-rotational Model

1) Axial Deflection Modeling:

Without losing the generality, this article provides a 2-dimensional(D) modeling, closely following the concept of co-rotational modeling given by Crisfield [18] and Yaw [19], where any targeted structure can be modeled as a combination of elastic elements. For instance, a slender beam is treated as a serial combination of small beam elements. By separating the local deformation of each beam element and its rigid motion, and allowing arbitrary large motions between adjacent beam elements, the co-rotational approach can model the large deformation of objects with sufficient accuracy and efficiency. As illustrated in Figure 2, each beam element has two nodes, node 1 and node 2, respectively. In the global coordinate frame O, X, Y , given the initial coordinates for two ends of beams (X_1, Y_1) and (X_2, Y_2) , the initial angle β_0 , as well as length L_0 of the beam can be derived accordingly. When the beam element changes to its current configuration under an external load, assuming node 1 and node 2 generate the displacements, (u_1, w_1) and (u_2, w_2) , respectively, the current incline angle β and length L can be derived, see Eqns. (2-3)

$$L_0 = \sqrt{(X_2 - X_1)^2 + (Y_2 - Y_1)^2} \quad (1)$$

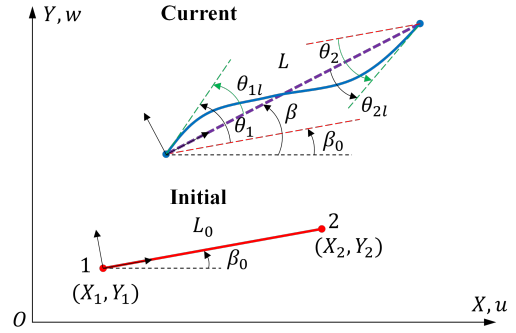


Figure 2: Relationship between global coordinates and local coordinates of the nodes of each beam element.

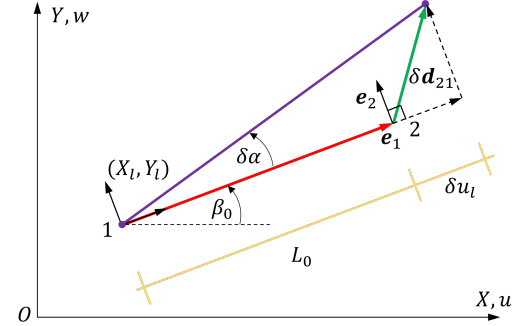


Figure 3: The global displacement for a beam element. (X_1, Y_1) represents the node coordinate in the local coordinate reference frame, where (e_1, e_2) is the unit vector: e_1 is along the beam and e_2 is perpendicular to the beam; the purple line represents the beam after a certain displacement; δd_{21} denotes the displacement vector; δu_l is the local translation displacement; $\delta \alpha$ represents the rotation angle of the beam.

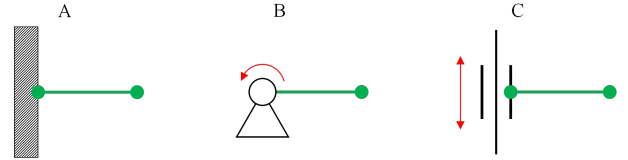


Figure 4: Typical types of support nodes. The support node displacement is $(u = 0, w = 0, \theta = 0)$ in (A), $(u = 0, w = 0, \theta \neq 0)$ in (B), $(u = 0, w \neq 0, \theta = 0)$ in (C).

$$\begin{aligned} dX &= (X_2 + u_2) - (X_1 + u_1) \\ dY &= (Y_2 + w_2) - (Y_1 + w_1) \end{aligned} \quad (2)$$

$$\begin{aligned} L &= \sqrt{(dX)^2 + (dY)^2} \\ \cos \beta &= \frac{dX}{L}, \sin \beta = \frac{dY}{L} \end{aligned} \quad (3)$$

With the resultant axial deformation $u_l = L - L_0$, the axial force N along the beam can be derived via

$$N = \frac{EAu_l}{L_0} \quad (4)$$

where E represents the module of elasticity and A denotes the cross-sectional area of the beam.

2) Rotational deflection modeling:

Apart from the axial deflection, each beam element also undertakes rotational motions at its two nodes. As shown in Fig. 2, θ_1 and θ_2 are the rotations of nodes 1 and 2, measured from the initial incline axis of the beam element. Together with node displacements, the global displacement of each node can

be represented by the vector θ_1 and θ_2 . Therefore, the local nodal rotations become

$$\begin{aligned}\theta_{1l} &= \theta_1 + \beta_0 - \beta \\ \theta_{2l} &= \theta_2 + \beta_0 - \beta\end{aligned}\quad (5)$$

Using the standard structural analysis results [20], the node moments of the beam (the moment of inertia is represented by I) can be related to the local nodal rotations with

$$\begin{Bmatrix} M_1 \\ M_2 \end{Bmatrix} = \frac{2EI}{L_0} \begin{bmatrix} 2 & 1 \\ 1 & 2 \end{bmatrix} \begin{Bmatrix} \theta_{1l} \\ \theta_{2l} \end{Bmatrix}\quad (6)$$

As a result, for a beam element, its global displacement (u, w, θ) can be used for calculating the local displacement $(\theta_{1l}, \theta_{2l}, u_l)$, and the latter can be further utilized to calculate the applied load (N, M_1, M_2) through Eqns.(1-6). This lays the foundation of the co-rotational modeling [18], [19].

3) *Variationally consistent tangent stiffness matrix:*

As illustrated in Fig.3, we have the following equation as

$$\delta u_l = \mathbf{e}_1^T \delta \mathbf{d}_{21} = \mathbf{r}^T \delta \mathbf{p}\quad (7)$$

with $\delta \mathbf{p}$ the variation of the global displacement vector $\mathbf{p} = [u_1 \ w_1 \ \theta_1 \ u_2 \ w_2 \ \theta_2]^T$ and $\mathbf{r} = [-\cos \beta \ -\sin \beta \ 0 \ \cos \beta \ \sin \beta \ 0]^T$. When $\delta \alpha$ is small, we have

$$\delta \alpha = \sin \delta \alpha = \frac{1}{L} \mathbf{e}_2^T \delta \mathbf{d}_{21} = \frac{1}{L} \mathbf{z}^T \delta \mathbf{p}\quad (8)$$

where $\mathbf{z} = [\sin \beta \ -\cos \beta \ 0 \ -\sin \beta \ \cos \beta \ 0]^T$. The changes of rotations can be provided as follows,

$$\delta \theta_l = \begin{Bmatrix} \delta \theta_{1l} \\ \delta \theta_{2l} \end{Bmatrix} = \begin{Bmatrix} \delta \theta_1 - \delta \alpha \\ \delta \theta_2 - \delta \alpha \end{Bmatrix} = \left[T - \frac{1}{L} \begin{bmatrix} \mathbf{z}^T \\ \mathbf{z}^T \end{bmatrix} \right] \delta \mathbf{p}\quad (9)$$

where $T = \begin{bmatrix} 0 & 0 & 1 & 0 & 0 & 0 \\ 0 & 0 & 0 & 0 & 0 & 1 \end{bmatrix}$. The change $\delta \mathbf{p}_l$ of the local displacement \mathbf{p}_l can be described concerning the change $\delta \mathbf{p}$ of the global displacement vector \mathbf{p} as

$$\delta \mathbf{p}_l = \begin{Bmatrix} \delta u_l \\ \delta \theta_{1l} \\ \delta \theta_{2l} \end{Bmatrix} = \mathbf{B} \delta \mathbf{p}\quad (10)$$

where \mathbf{B} is the transformation matrix and has the following form

$$\mathbf{B} = \begin{bmatrix} -\cos \beta & -\sin \beta & 0 & \cos \beta & \sin \beta & 0 \\ -\frac{\sin \beta}{L} & \frac{\cos \beta}{L} & 1 & \frac{\sin \beta}{L} & -\frac{\cos \beta}{L} & 0 \\ -\frac{\sin \beta}{L} & \frac{\cos \beta}{L} & 0 & \frac{\sin \beta}{L} & -\frac{\cos \beta}{L} & 1 \end{bmatrix}\quad (11)$$

In the local coordinate frame $\{X_l, Y_l\}$, the local internal force vector of the element i can be described by $\mathbf{q}_i = [N \ M_1 \ M_2]^T$ and the local virtual displacement is $\delta \mathbf{p}_{lv} = [\delta u_{lv} \ \delta \theta_{1lv} \ \delta \theta_{2lv}]^T$. In terms of the global coordinate frame $\{X, Y\}$, \mathbf{q}_i is the vector of global internal forces for the element i and $\delta \mathbf{p}_v$ are the arbitrary virtual displacements. For each beam element, according to the equivalence of virtual work in the local and global systems, we have

$$\delta \mathbf{p}_v^T \mathbf{q}_i = \delta \mathbf{p}_{lv}^T \mathbf{q}_{li} = (\mathbf{B} \delta \mathbf{p}_v)^T \mathbf{q}_{li} = \delta \mathbf{p}_v^T \mathbf{B}^T \mathbf{q}_{li}\quad (12)$$

Namely,

$$\mathbf{q}_i = \mathbf{B}^T \mathbf{q}_{li}\quad (13)$$

Then, the vector F_{int} of internal global forces is provided as

$$F_{int} = A_{s_{i=1}}^{n_m} \mathbf{q}_i = \sum_{i=1}^{n_m} \left[\cdots \ \mathbf{q}_{i,1} \ \mathbf{q}_{i,2} \ \mathbf{q}_{i,3} \ \cdots \ \mathbf{q}_{i,4} \ \mathbf{q}_{i,5} \ \mathbf{q}_{i,6} \ \cdots \right]^T\quad (14)$$

where A_s is the assembly index (see Hughes[21]). Taking the derivative of $\mathbf{q}_i = \mathbf{B}^T \mathbf{q}_{li}$, we have

$$\delta \mathbf{q}_i = \mathbf{k}_i \delta \mathbf{p}\quad (15)$$

in which \mathbf{k}_i is the tangent stiffness matrix. The detailed calculations are omitted here and the readers can refer to [18], [19]. Here the final formula of \mathbf{k}_i is given as

$$\mathbf{k}_i = \mathbf{B}^T \mathbf{C}_l \mathbf{B} + \frac{F_N}{L} / \mathbf{z} \mathbf{z}^T + \frac{M_1 + M_2}{L^2} (\mathbf{r} \mathbf{z}^T + \mathbf{z} \mathbf{r}^T)\quad (16)$$

where

$$\mathbf{C}_l = \frac{EA}{L_0} \begin{bmatrix} 1 & 0 & 0 \\ 0 & \frac{4I}{A} & \frac{2I}{A} \\ 0 & \frac{2I}{A} & \frac{4I}{A} \end{bmatrix}\quad (17)$$

Then we can further calculate the global tangent stiffness matrix \mathbf{K} of the whole structure as

$$\mathbf{K} = A_{s_{i=1}}^{n_m} \mathbf{k}_i = A_{i=1}^{n_m} \begin{bmatrix} \vdots & \vdots \\ \cdots & k_{1,1}^i & \cdots & k_{1,2}^i & \cdots \\ \vdots & \vdots \\ \cdots & k_{2,1}^i & \cdots & k_{2,2}^i & \cdots \\ \vdots & \vdots \end{bmatrix}\quad (18)$$

A_s is the assembly operator and n_m is the number of elements. The assembly rows and columns of \mathbf{k}_i depend on the order of the first and second nodes in the element i . Allowing for the node supports, \mathbf{K} is changed to the modified global tangent stiffness matrix \mathbf{K}_s . Figure 4 presents typical types of support nodes that are constrained depending on the support conditions. The displacements in the constrained directions are always zero for a particular support node regardless of external forces. The rows and columns of \mathbf{K}_s concerning this displacement will be zero since the displacement on the support node is still zero. For example, if node i is defined as one support node and fully constrained, then the elements in the related rows $(3i - 2, 3i - 1, 3i)$ and related columns $(3i - 2, 3i - 1, 3i)$ of \mathbf{K}_s are all set to be zero.

Algorithm 1 Member data update

Input:

$n_{nodes}, n_{mem}, m_{conn}, \mathbf{A}, \mathbf{E}, \mathbf{I}, x_0, y_0, L_0, \beta_0, \mathbf{u}, R_m$

Calculations:

For $i=1: n_{mem}$

 Obtain $L, \cos \beta, \sin \beta$ according to Eqns. (1-3)

 Obtain \mathbf{q}_{li} according to Eqns. (4-8) and thus \mathbf{q}_i

 Obtain F_{int} according to Eqns. (13-16)

End

Output: $L, c, s, \mathbf{q}_l, F_{int}$

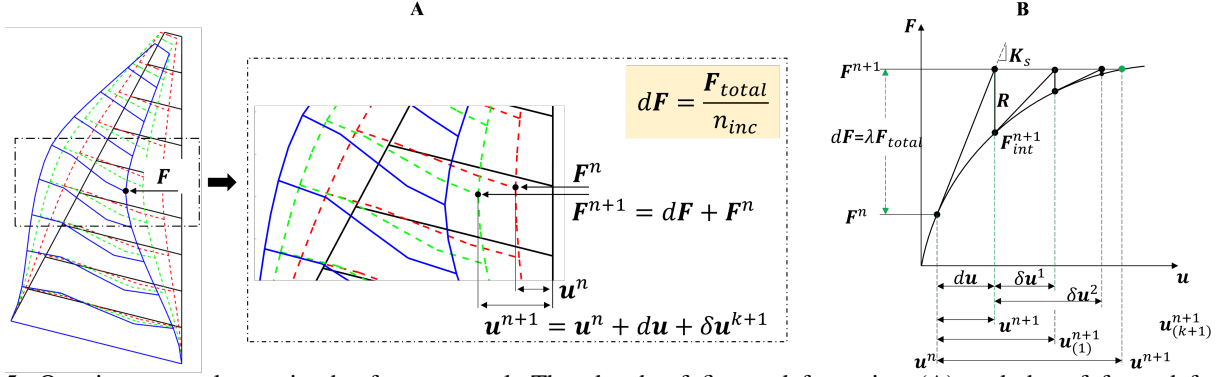


Figure 5: One incremental step in the force control. The sketch of finger deformation (A) and the of force-deformation relationship (B).

Algorithm 2 Tangent stiffness matrix update

Input:

$n_{nodes}, n_{mem}, m_{conn}, sup, A, E, I, L, c, s, q_l, R_m$

Calculations:

For $i=1: n_{mem}$

 Obtain K according to Eqns. (9-20)

 Obtain the modified K_s based on the support condition sup

End

Output: K_s

B. Force Control

“Force control” indicates that the displacement is calculated by the contact force. In this subsection, we describe how to calculate the displacement on a finger of a gripper. This is an implicit formulation that uses the algorithm of Newton-Raphson iterations at the global level to achieve equilibrium during each incremental load step [22]. Different from the linear analysis, in the force control described here, the total increment is subdivided into a number of steps, with each represented by a cycle in which an equilibrium is reached within a certain tolerance. Specifically, the total vector of externally applied global nodal forces F_{total} is defined as a $3n_m \times 1$ vector, where the non-zero elements represent the externally applied forces at the selected nodes, allowing for flexible force representation of either concentrated load or distributed loads with no constraints. Here we consider that a total number n_{inc} of load increment steps is required to reach the final equilibrium from the initial equilibrium, and a load of each increment is dF . Thus, we have

$$dF = \lambda F_{total} \quad (19)$$

with load ratio $\lambda = 1/n_{inc}$. Especially, in the n^{th} increment, we define the vector of global nodal displacements as u^n and the vector of global nodal forces as F^n . According to **Algorithm 1** and **Algorithm 2**, we can calculate L, c, s, q_l, F_{int} and obtain the modified stiffness matrix K_s . Then, the vector du of each incremental global nodal displacement can be calculated using K_s [18] as

$$du = K_s^{-1} dF \quad (20)$$

As shown in Fig.5, u^n and F^n can be further updated with

$$\begin{aligned} u^{n+1} &= u^n + du + \delta u^{k+1} \\ F^{n+1} &= F^n + dF \end{aligned} \quad (21)$$

which will later be used in the iteration cycle to achieve equilibrium. Further, we can update $L, c, s, q_l^{n+1}, F_{int}^{n+1}$ according to **Algorithm 1** based on u^{n+1} . For the iterations, we need to determine the deviation that can be accepted to compare with a set tolerance by defining the residual R as

$$\begin{aligned} R &= F_{int}^{n+1} - F^{n+1} \\ R &= \sqrt{R \cdot R} \end{aligned} \quad (22)$$

Following the initial preparation process, we enter the iteration cycle, aiming to reach the force equilibrium. A few iteration variables are defined as the iteration number $k = 0, tolerance = 10^{-3}$. The maximum iteration step is limited by $maxiter = 100$. The correction to incremental global nodal displacements is defined as $\delta u^k = 0$. The temporary vector of local forces in the k -th iteration cycle is set as

$$q_{l-temp}^k = q_l^{n+1} \quad (23)$$

In each step k , firstly, the stiffness matrix K_s is updated according to **Algorithm 2** based on updated current values of inputs and q_{l-temp}^k . Then the global nodal displacements and member data are updated as

$$\begin{aligned} \delta u^{k+1} &= \delta u^k - K_s^{-1} R \\ u_{(k+1)}^{n+1} &= u^n + du + \delta u^{k+1} \end{aligned} \quad (24)$$

where $u_{(k+1)}^{n+1}$ represents u^{n+1} in the $(k+1)$ -th iteration. When the loop is stopped, $u_{(k+1)}^{n+1}$ becomes u^{n+1} .

Updating the $q_{l-temp}^k, F_{int}^{n+1}$ according to **Algorithm 1** based on $u_{(k+1)}^{n+1}$ is obtained in Eqn.(23) and the new residual R is updated using Eqn.(22). Updating iteration number $k = k + 1$, the iteration cycle will terminate if $R \leq tolerance$ or $k \geq maxiter$ (in this case, the convergence criteria are not met), and the variables will update to their final value in this n -th increment.

$$\begin{aligned} q_l^{n+1} &= q_{l-temp}^{k+1} \\ u^{n+1} &= u_{(k+1)}^{n+1} = u^n + du + \delta u^{k+1} \end{aligned} \quad (25)$$

The complete force control in the n^{th} increment is also illustrated in Figure.5, where the variables updated in both the preliminary step and iteration cycle are demonstrated. The detailed algorithm is illustrated in **Algorithm 3**

III. SIMULATION EXPERIMENTS

This section emphasizes applying the proposed co-rotational modeling approach to optimize key design parameters in developing a Fin-Ray gripper. A family of Fin-Ray grippers

Algorithm 3 Force Control

Input:
 $n_{nodes}, n_{mem}, m_{conn}, \mathbf{A}, \mathbf{E}, \mathbf{I}, \mathbf{x}_0, \mathbf{y}_0, \mathbf{L}_0, \beta_0, \mathbf{u}, R_m, \mathbf{F}_{total}$
Calculations:**For** $n=1: n_{mem}$ calculate $d\mathbf{F}$ by Eqn.(19)calculate $\mathbf{L}, \mathbf{c}, \mathbf{s}, \mathbf{q}_l, \mathbf{F}_{int}$ by **Algorithm 1**calculate \mathbf{K}_s by **Algorithm 2**Obtain \mathbf{d}_u according to Eqn.(20)update \mathbf{u}^{n+1} and \mathbf{F}^{n+1} by Eqn.(21)update $\mathbf{L}, \mathbf{c}, \mathbf{s}, \mathbf{q}_l^{n+1}, \mathbf{F}_{int}^{n+1}$ by **Algorithm 1** based on \mathbf{u}^{n+1} calculate the residual \mathbf{R} by Eqn.(22)set up iteration variables $k, tolerance, maxiter, \delta\mathbf{u}$ and \mathbf{q}_l^{k-temp} start iterations while $R \geq tolerance$ and $k \leq maxiter$ i. calculate \mathbf{K}_s by **Algorithm 2** and \mathbf{q}_l^{k-temp} by Eqn.(23)ii. update member data $\delta\mathbf{u}^{k+1}$ and $\mathbf{u}^{(k+1)}$ by Eqn.(24)iii. update $\mathbf{q}_l^{k+1-temp}, \mathbf{F}_{int}^{k+1}$ by **Algorithm 1** based on $\mathbf{u}_{current}$ iv. calculate the residual \mathbf{R} and R by Eqn.(22)v. update iteration number $k=k+1$

End of while loop iterations

Update variables \mathbf{q}_l^{n+1} and \mathbf{u}^{n+1} by Eqn. (25)**End****Output:** $\mathbf{q}_l^{n+1}, \mathbf{u}^{n+1}$

with various design parameters are considered respectively, and their performances are evaluated based on whether they accurately capture displacements under external forces or not. Simulation experiments are conducted and analyzed by comparing the proposed approach with Finite Element Analysis (FEA), a crucial benchmark solution for the numerical analysis of mechanical models. Here a given compliant finger is meshed by nodes, with the material parameters summarized in Table I.

Table I: The parameters of the models used in the design characterization

Item	Value
Width m (m)	$40e^{-3}$
Height n (m)	$72e^{-3}$
Cross section of each member (b, h) (m)	$20e^{-3}, 1e^{-3}$
Young's modules (Pa)	$2e^7$

Four main design parameters are taken into consideration, such as (1) the number of crossbeams jointing the front contact and back contact sides, regardless of rigid or soft crossbeams; (2) the top angle between the front Fin-Ray and back one; (3) the inclination angle of the crossbeams; (4) connection type between crossbeams and front-back Fin-Rays. Specially, we distinguish between two types of connection: the crossbeam element that can freely rotate around the connection is defined as the "simple" connection, while the "rigid" connection indicates that crossbeams and front-back Fin-Rays are fixed to each other.

A. The number of crossbeams

Figure.6 presents the force-to-displacement simulation of Fin-Ray fingers with 3, 4, or 5 crossbeams. The forces with

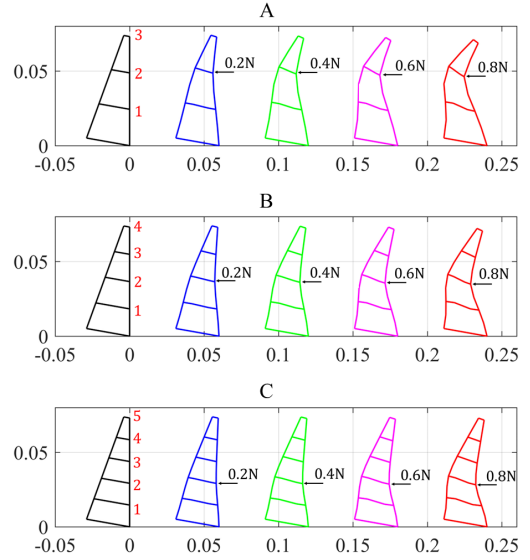


Figure 6: The deformations of three Fin-Ray fingers with different numbers of crossbeams such as 2(A), 3(B) and 4(C).

Table II: Evaluations on the numbers of crossbeams.

	Force	0.2N	0.4N	0.6N	0.8N	
2	Node	Error ratio(%)				Ave. ¹ (%)
	1 st	-9.0	-11.5	-12.0	-13.2	11.4
	2 nd	-3.0	-3.3	-4.1	-5.5	4.0
	3 rd	3.9	3.6	7.3	N.A. ²	5.0
	Ave. ¹ (%)	5.3	6.1	7.8	9.35	6.8
3	Node	Error ratio(%)				Ave. ¹ (%)
	1 st	-12.9	-11.6	-11.4	-12.4	12.1
	2 nd	-2.6	-4.0	-5.3	-5.8	4.4
	3 rd	4.0	1.0	1.7	0.5	1.8
	4 th	9.9	7.5	8.3	10.2	9.0
Ave. ¹ (%)	7.4	6.0	6.7	7.2	6.8	
4	Node	Error ratio(%)				Ave. ¹ (%)
	1 st	-11.4	-7.9	-8.5	-9.2	9.3
	2 nd	-2.7	-1.9	-2.3	-4.3	2.8
	3 rd	0.0	0.7	0.2	-0.6	0.4
	4 th	7.5	5.4	6.7	6.7	6.6
5 th	12.0	10.1	11.1	12.1	11.0	
Ave. ¹ (%)	6.7	5.2	5.8	6.6	6.1	

Ave.¹ indicate the average value; N.A.² represents that the FE method is invalid.

a magnitude of 0.2N, 0.4N, 0.6N, and 0.8N are applied at the selected nodes. Regardless of the number of crossbeams, the centering node(s) of the Fin-Ray finger generate(s) the maximum deformation while only slight deformation happens at the peripheral nodes. Considering all three fingers with different numbers of crossbeams, it is noted that the overall stiffness increases with the rise in the number of crossbeams, providing smaller deformation under given loads. Additionally, we define the force causing collapses of the finger's structure as the maximum allowable force that prevents the gripper from reaching an unstable status. We gradually increase the force load that is applied at the node. In this case, the maximum allowable forces of type 1 (2 crossbeams), type 2 (3 crossbeams), and type 3 (4 crossbeams) are 0.8N, 1.2N, and 1.9N, respectively.

Further, the discrepancies between the displacements gen-

erated from mathematical models and FEA simulations are calculated and listed in Table.II. In particular, the error at the top and bottom nodes are around 10%, and the middle nodes are below 10%. The results reveal that the number of crossbeams significantly affects the deformed shape of the Fin-Ray structure and the maximum allowable force that can keep the stability of the structure. Specifically, a gripper with Fin-Rays, including fewer rigid ribs, can perform enveloping grasping through wrapping with a heavily deformed Fin-Ray finger. By contrast, the increase in the number of crossbeams enables the gripper to bend smoothly under concentrated loads due to a bigger stiffness, which ensures a stable grasp; Whereas, this can also be a problem when grasping soft or fragile objects as high-stiffness Fin-Ray structure may cause damage. A remarkable finding is that the proposed displacement-force model performs better with the increasing number of crossbeams. Thus, after doing a trade-off of the bent deformation and stiffness of the Fin-Ray structure, we prefer to increase the number of crossbeams to improve the estimation accuracy of displacement and force for the proposed model and avoid the risk of undesirable instabilities. With the influence determined, for simplicity, we choose the gripper with 4 crossbeams in the following experiments.

B. The top angle

The force-to-displacement simulation of Fin-Ray fingers with various top angles is presented. Three representative angles are selected (20° , 30° , and 40°). Force loads are, in turn, applied at each node. Fig.7 reveals the case when force is exerted at node 2, as it generates big enough deformation under a maximum force of 0.8N. Generally, among three fingers, the maximum deformation under the same force load increases along with the increase of top angle, which is true of nodes 1, 2, and 3 except for node 4. In terms of practical application, a large top angle is desirable so that a gripper can generate big enough deformation to hold objects. The maximum allowable forces for 40° , 30° , and 20° are 1.8N, 1.6N, and 1.2N, respectively, which suggests a soft gripper with a larger top angle that has better resistance to collapse. However, this will increase the overall weight of the gripper. Thus, optimal design can be conducted in the trade-off of the elasticity, overall size as well as the weight of the gripper.

From the comparison results, we witness that the proposed co-rotational model can obtain relatively accurate displacements despite of different top angles of the Fin-Ray structure. The error at nodes 1 and 4 are relatively more significant (around 10%), and nodes 2 and 3 are smaller (around 6%).

C. The inclination of the crossbeams

This subsection presents the force-to-displacement simulation of Fin-Ray grippers with various crossbeam inclination angles. Three representative inclination angles of crossbeams are selected, such as -10° , 0° , and $+10^\circ$. External force loads with a maximum magnitude of 0.8N are applied at four nodes in sequence. Similarly, we present the case when forces are exerted at node 2 (see Fig.8). For each Fin-Ray finger, the deformation increases with the improvement of force magnitude. Generally, among three fingers, with the increase

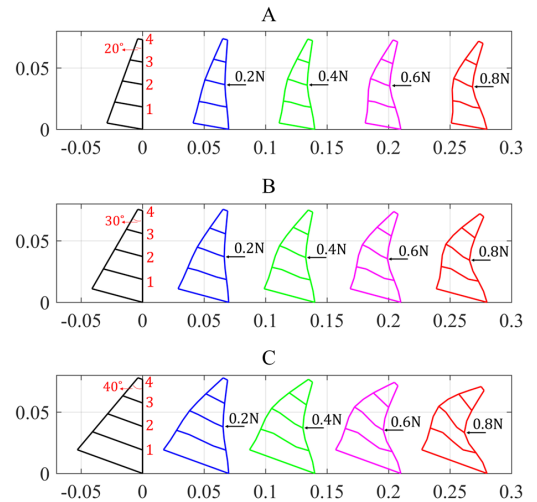


Figure 7: The deformations of three Fin-Ray fingers with different top angles such as 20° (A), 30° (B) and 40° (C). The external forces are applied at node 2.

Table III: Evaluations on the top angle of crossbeams.

	Force	0.2N	0.4N	0.6N	0.8N	
20°	Node	Error ratio(%)				Ave. ¹ (%)
	1 st	-12.9	-11.6	-11.4	-12.4	12.1
	2 nd	-2.6	-4.0	-5.3	-5.8	4.4
	3 rd	4.0	1.0	1.7	0.5	1.8
	4 th	9.9	7.5	8.3	10.2	9.0
	Ave. ¹ (%)	5.3	6.1	7.8	9.35	6.8
30°	Force	0.2N	0.4N	0.6N	0.8N	
	Node	Error ratio(%)				Ave. ¹ (%)
	1 st	-14.1	-9.3	-9.5	-9.5	10.6
	2 nd	-3.8	-4.8	-5.8	-6.8	5.3
	3 rd	0.7	-0.5	-1.1	-2.6	1.2
	4 th	4.7	3.9	5.4	8.0	5.5
Ave. ¹ (%)	5.8	4.6	5.5	6.7	5.7	
40°	Force	0.2N	0.4N	0.6N	0.8N	
	Node	Error ratio(%)				Ave. ¹ (%)
	1 st	-11.7	-9.4	-11.5	-13.3	11.5
	2 nd	-5.0	-6.3	-7.5	-9.5	7.1
	3 rd	-2.0	-3.5	-4.6	-5.0	3.8
	4 th	2.3	0	1.0	4.4	1.9
Ave. ¹ (%)	5.3	4.8	6.2	8.1	6.1	

Ave.¹ indicate the average value.

of inclination angle, the maximum deformation under the same force load also increases, which is true of the cases for nodes 2, 3, and except node 1.

It is noted that the ribs' inclination significantly affects the proposed model's overall behavior. Under the same load at the same node, the Fin-Ray finger, including ribs with a $+10^\circ$ inclination angle, generates the biggest displacement (except for node 1), implying a lower stiffness. The finger that includes ribs with -10° forms the smallest displacement, revealing a higher stiffness. The instability forces for the three cases are -10° (1.15N), $+10^\circ$ (1.35N), and 0° (1.2N). Compared to -10° , $+10^\circ$ has a 10% bigger displacement and 14.5% higher instability force.

Table IV presents the discrepancies between the proposed model and FEA. The average error rates are similar among the three cases (around 7%). The geometrical configurations of crossbeams with different inclinations do not generate obvious

effects on the accuracy of the proposed co-rotational model. The gripper with a negative incline angle has a bigger stiffness, resulting in a bigger buckling force. For each type, we repeat the loading force at all 4 nodes. The error at nodes 1 and 4 are relatively bigger (around 10%), and nodes 2 and 3 are smaller (around 5%).

D. Connection type

The effects of connection types between middle crossbeams and front and back sides of Fin-Rays are simulated. Again, results from the proposed co-rotational model and FEA simulation are compared (see Table.V). As is demonstrated, the gripper with a simple connection generates almost twice the deformation of the gripper with a rigid connection under the same load. For example, the displacements of nodes 2 and 3 are 22.9mm and 23.5mm with simple connections, compared to 11mm and 9.8mm with the rigid connection when subjected to 0.8N force at node 2.

It should be found that the co-rotational model applied to these two connection types is accurate and resembles very closely. The error rate at nodes 1 and 4 are relatively bigger (around 10%), and nodes 2 and 3 are smaller (around 5%). The Fin-Ray finger with the simple connection generates almost three-time bigger displacements than one with the rigid connection, undertaking the same load at the same node. Whereas for rigid connections, the same deformed shapes are obtained by a drastically lower force. In addition, a rigid connection demonstrates a higher maximum allowable force (1.2N) compared to a simple connection (0.7N).

E. Discussion

The influence of four parameters is compared and summarized here. First, it is found that the inclination of crossbeams is the most decisive parameter that influences the overall performance of both grippers in stiffness and instability force. A positive inclination angle brings about a more compliant closing (lower stiffness), generating larger deformation under the same load and allowing higher contact force than a negative one. Thus, the priority should be given during the new gripper design. Meanwhile, though simple connections endow the gripper with a lower stiffness, it significantly weakens its strength in resisting instability. In real scenarios, the optimized design should be closely related to the application, carefully considering the trade-off between stiffness and force.

The proposed modeling accurately captures the finger deformation under external loads, with an average error ratio $\leq 10\%$ and, in particular, 6% for the centering nodes. This is particularly important from an optimization point of view, as the centering nodes will be more used in practical applications. The small average error ratio implies that it is possible to focus the investigation on the finger design with the proposed force-displacement mapping.

IV. CONCLUSIONS

For the first time, this article constructs a bidirectional universal model that mutually maps finger deformation and external contact force, simultaneously facilitating design optimization and ensuring force-aware grasping (Part I and Part II). In Part I, the theoretical modeling of beam element employing

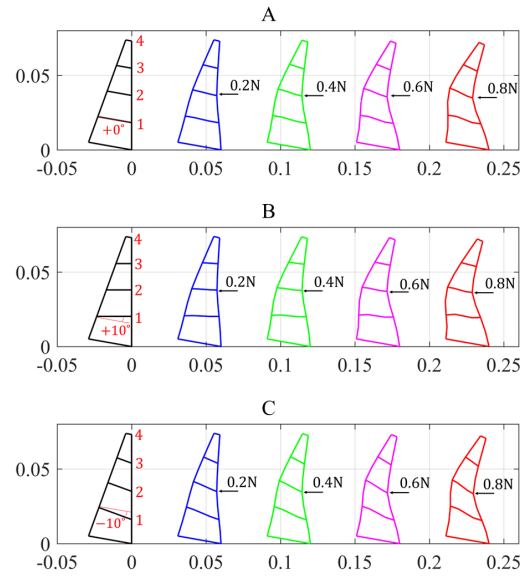


Figure 8: The deformations of three Fin-Ray fingers with different inclination angles, such as 0° (A), 10° (B) and -10° (C).

Table IV: Evaluations on the inclination of crossbeams.

	Force	0.2N	0.4N	0.6N	0.8N	
0°	Node	Error ratio(%)				Ave. ¹ (%)
	1 st	-12.9	-11.6	-11.4	-12.4	12.1
	2 nd	-2.6	-4.0	-5.3	-5.8	4.4
	3 rd	4.0	1.0	1.7	0.5	1.8
	4 th	9.9	7.5	8.3	10.2	9.0
	Ave. ¹ (%)	7.4	6.0	6.7	7.2	6.8
$+10^\circ$	Force	0.2N	0.4N	0.6N	0.8N	
	Node	Error ratio(%)				Ave. ¹ (%)
	1 st	-8.1	-8.2	-9.2	-10.0	8.9
	2 nd	-3.5	-1.3	-3.2	-3.7	2.9
	3 rd	1.2	3.4	2.6	1.9	2.3
	4 th	11.5	6.8	8.6	11.3	9.6
Ave. ¹ (%)	6.1	4.9	5.9	6.8	5.9	
-10°	Force	0.2N	0.4N	0.6N	0.8N	
	Node	Error ratio(%)				Ave. ¹ (%)
	1 st	-9.2	-9.7	-11.4	-12.6	10.7
	2 nd	-1.1	-3.3	-4.6	-5.4	3.6
	3 rd	3.1	1.8	1.8	0.6	1.8
	4 th	9.1	5.8	8.3	8.5	7.9
Ave. ¹ (%)	5.6	5.2	6.5	6.8	6.0	

Ave.¹ indicate the average value.

the co-rotational concept is presented, with few assumptions needed and high computational efficiency. We further propose a force-displacement algorithm depicting finger deformation under external forces, which is then experimentally validated in simulations. Results reveal that the proposed method properly describes the force-deformation mapping, with an average error ratio below 10% compared with FEA. In particular, insights into the influence of four key design parameters for Fin-Ray grippers' performance have been provided, facilitating future works regarding gripper design optimization. Part II of this article presents a displacement algorithm that measures contact forces and influence of modeling parameters, providing further verification of the proposed model and a novel mathematical tool for force control of more compliant grippers sensor-free.

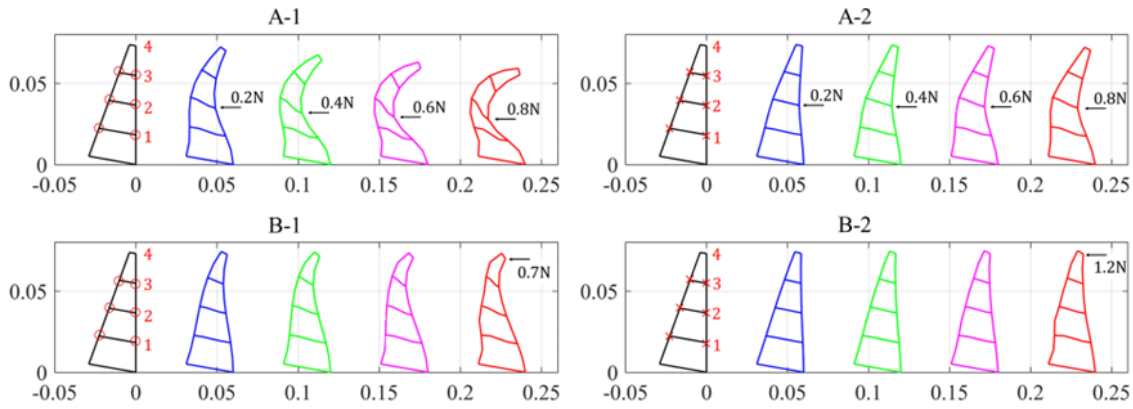


Figure 9: The deformations of Fin-Ray fingers with two connection types, including “simple” (A-1, B-1) and “rigid” (A-2, B-2) connections.

Table V: Evaluations on the two connection types for the Fin-Ray finger.

	Force	0.2N	0.4N	0.6N	0.8N		Force	0.2N	0.4N	0.6N	0.8N		
S.connection	Node	Error ratio(%)				A. ² (%)	F.connection	Node	Error ratio(%)				A. ² (%)
	1 st	-5.8	-9.2	-10.5	-11.5	9.3		1 st	-12.9	-11.6	-11.4	-12.4	12.1
	2 nd	-1.9	-3.5	-3.5	-3.2	3.0		2 nd	-2.6	-4.0	-5.3	-5.8	4.4
	3 rd	0.2	-0.5	-0.9	0.0	0.4		3 rd	4.0	1.0	1.7	0.5	1.8
	4 th	3.8	6.6	9.9	N.A. ³	6.8		4 th	9.9	7.5	8.3	10.2	9.0
	A. ² (%)	2.9	5.0	6.2	4.9	4.9		A. ² (%)	7.4	6.0	6.7	7.2	6.8

S. and F. represent “Simple” and “Fixed”, respectively. Ave.¹ indicates the average values; N.A.³ represents that the FE method is invalid.

REFERENCES

- [1] H. Dong, E. Asadi, G. Sun, D. K. Prasad, and I.-M. Chen, “Real-time robotic manipulation of cylindrical objects in dynamic scenarios through elliptic shape primitives,” *IEEE Transactions on Robotics*, vol. 35, no. 1, pp. 95–113, 2019.
- [2] H. Dong, D. K. Prasad, and I.-M. Chen, “Object pose estimation via pruned hough forest with combined split schemes for robotic grasp,” *IEEE Transactions on Automation Science and Engineering*, vol. 18, no. 4, pp. 1814–1821, 2021.
- [3] H. Dong, E. Asadi, C. Qiu, J. Dai, and I.-M. Chen, “Geometric design optimization of an under-actuated tendon-driven robotic gripper,” en, *Robotics and Computer-Integrated Manufacturing*, vol. 50, pp. 80–89, Apr. 2018.
- [4] X. Shan and L. Birglen, “Modeling and analysis of soft robotic fingers using the fin ray effect,” en, *The International Journal of Robotics Research*, vol. 39, no. 14, pp. 1686–1705, Dec. 2020.
- [5] H. Dong, C.-Y. Chen, C. Qiu, C.-H. Yeow, and H. Yu, “Gsg: A granary-shaped soft gripper with mechanical sensing via snap-through structure,” *IEEE Robotics and Automation Letters*, vol. 7, no. 4, pp. 9421–9428, 2022.
- [6] T. Nishimura, K. Mizushima, Y. Suzuki, T. Tsuji, and T. Watanabe, “Variable-grasping-mode underactuated soft gripper with environmental contact-based operation,” *IEEE Robotics and Automation Letters*, vol. 2, no. 2, pp. 1164–1171, 2017.
- [7] M. Catalano, G. Grioli, E. Farnioli, A. Serio, C. Piazza, and A. Bicchi, “Adaptive synergies for the design and control of the Pisa/IIT SoftHand,” en, *The International Journal of Robotics Research*, vol. 33, no. 5, pp. 768–782, Apr. 2014.
- [8] A. M. Dollar and R. D. Howe, “The highly adaptive sdm hand: Design and performance evaluation,” *The international journal of robotics research*, vol. 29, no. 5, pp. 585–597, 2010.
- [9] R. Deimel and O. Brock, “A compliant hand based on a novel pneumatic actuator,” in *2013 IEEE International Conference on Robotics and Automation*, 2013, pp. 2047–2053.
- [10] J. M. Krahn, F. Fabbro, and C. Menon, “A soft-touch gripper for grasping delicate objects,” *IEEE/ASME Transactions on Mechatronics*, vol. 22, no. 3, pp. 1276–1286, 2017.
- [11] J. R. Amend, E. Brown, N. Rodenberg, H. M. Jaeger, and H. Lipson, “A positive pressure universal gripper based on the jamming of granular material,” *IEEE Transactions on Robotics*, vol. 28, no. 2, pp. 341–350, 2012.
- [12] T. G. Thuruthel, S. Haider Abidi, M. Cianchetti, C. Laschi, and E. Falotico, “A bistable soft gripper with mechanically embedded sensing and actuation for fast grasping,” in *2020 29th IEEE International Conference on Robot and Human Interactive Communication (RO-MAN)*, 2020, pp. 1049–1054.
- [13] W. Xu, H. Zhang, H. Yuan, and B. Liang, “A compliant adaptive gripper and its intrinsic force sensing method,” *IEEE Transactions on Robotics*, vol. 37, no. 5, pp. 1584–1603, 2021.
- [14] D. Yoon and Y. Choi, “Analysis of fingertip force vector for pinch-lifting gripper with robust adaptation to environments,” *IEEE Transactions on Robotics*, vol. 37, no. 4, pp. 1127–1143, 2021.
- [15] J. Till and D. C. Rucker, “Elastic stability of cosserat rods and parallel continuum robots,” *IEEE Transactions on Robotics*, vol. 33, no. 3, pp. 718–733, 2017.
- [16] C. Armanini, I. Hussain, M. Z. Iqbal, D. Gan, D. Praticchizzo, and F. Renda, “Discrete cosserat approach for closed-chain soft robots: Application to the fin-ray finger,” *IEEE Transactions on Robotics*, vol. 37, no. 6, pp. 2083–2098, 2021.
- [17] H. Dong, E. Asadi, C. Qiu, J. Dai, and I.-M. Chen, “Grasp analysis and optimal design of robotic fingertip for two tendon-driven fingers,” en, *Mechanism and Machine Theory*, vol. 130, pp. 447–462, Dec. 2018.
- [18] R. De Borst, M. A. Crisfield, J. J. Remmers, and C. V. Verhoosel, *Nonlinear finite element analysis of solids and structures*. John Wiley & Sons, 2012.
- [19] L. L. Yaw, *Co-rotational meshfree formulation for large deformation inelastic analysis of two-dimensional structural systems*. University of California, Davis, 2008.
- [20] W. Spencer, *Fundamental structural analysis*. Springer Science & Business Media, 2013.
- [21] T. J. Hughes, *The finite element method: linear static and dynamic finite element analysis*. Courier Corporation, 2012.
- [22] M. Crisfield, “A faster modified newton-raphson iteration,” *Computer methods in applied mechanics and engineering*, vol. 20, no. 3, pp. 267–278, 1979.